Information Fusion Strategies for Collaborative Radio SLAM

Joshua Morales and Zaher M. Kassas
Department of Electrical and Computer Engineering
University of California, Riverside
{jmora047@ucr.edu, zkassas@ieee.org}

Abstract—**Information fusion strategies for navigation using signals of opportunity (SOPs) in a collaborative radio simultaneous and mapping (CoRSLAM) framework are studied. The following problem is considered. Multiple autonomous vehicles (AVs) with access to global navigation satellite system (GNSS) signals are aiding their on-board inertial navigation systems (INSs) with GNSS pseudoranges. While navigating, AV-mounted receivers draw pseudorange measurements on ambient unknown terrestrial SOPs and collaboratively estimate the SOPs' states. After some time, GNSS signals become unavailable, at which point the AVs use the SOPs to aid their INSs in a CoRSLAM framework. Two information fusion strategies are studied: (i) sharing time-of-arrival (TOA) measurements from SOPs and (ii) sharing time-difference-of-arrival (TDOA) measurements taken with reference to an SOP. Experimental results are presented demonstrating unmanned aerial vehicles (UAVs) navigating with the CoRSLAM framework, reducing the final localization error after 30 seconds of GPS unavailability from around 55 m to around 6 m.**

I. INTRODUCTION

Fully autonomous vehicles (AVs) must posses a reliable, accurate, and tamper-proof navigation system. Today's vehicular navigation systems couple a global navigation satellite system (GNSS) receiver with an inertial navigation system (INS) [1] and potentially other dead-reckening type sensors (e.g., lasers [2] and cameras [3]). Relying on GNSS poses an alarming vulnerability: GNSS signals could become unavailable or unreliable in environments such as deep urban canyons or environments experiencing a malicious attack (e.g., jamming or spoofing). Without GNSS aiding, the errors in the INS (and other dead-reckoning type sensors) will accumulate and eventually diverge, compromising the AV's safe operation. Introducing additional sensors may reduce the rate of error divergence; however, this may violate cost, size, weight, or power constraints.

Alternative to sensor-based approaches, signals of opportunity (SOPs) have been considered for navigation in the absence of GNSS signals [4]–[6]. SOPs (e.g., AM/FM radio [7], cellular [8]–[10], digital television [11], and iridium [12], [13]) are free to use and reduce the need for expensive and bulky aiding sensors. SOPs are abundant in GNSS-challenged environments, making them attractive aiding sources for an

INS whenever GNSS signals become unavailable [14]. However, unlike GNSS where the states of satellite vehicles (SVs) are readily available, the states of SOPs (positions, clock biases, and clock drifts) may not be known *a priori* and must be estimated [15].

Navigating in an SOP environment can be done in two frameworks: (1) a mapper/navigator framework in which some mapping AVs with knowledge of their own states estimate the states of the SOPs and share these estimates with navigating AVs that have no knowledge of their own states [16] or (2) a radio simultaneous localization and mapping (SLAM) framework, where the states of unknown SOPs are simultaneously estimated alongside the AV's states [17]. However, in contrast to the typical SLAM map which is composed of static states (e.g., positions of walls, poles, trees, etc.), the radio SLAM map is composed of dynamic stochastic states corresponding to the SOPs' clock errors (bias and drift).

Collaboration improves the navigation performance [18], [19]. In collaborative radio SLAM (CoRSLAM), collaborating AVs can improve their individual state estimates (attitude, position, velocity, clock bias, and clock drift) by sharing and fusing mutual measurements made on the dynamic stochastic signal map [20]. The question of how such information should be fused often arises during the design of any collaborative navigation architecture. This paper is the first to study this question in the context of aided-INS's in a CoRSLAM framework.

This paper makes two contributions. First, the estimation uncertainties of two fusion strategies in a CoRSLAM environment are compared: (i) time-of-arrival (TOA) and (ii) time-difference-of-arrival (TDOA) taken with reference to selected SOPs. Second, the dependence of the estimation performance on the TDOA SOP reference selection is studied. The use of TOA and TDOA in radionavigation and localization have been compared in other contexts. In [21], the use of GPS pseudoranges as TOA and TDOA were shown to yield identical localization results. In [22], the Cramér-Rao lower bound (CRLB) was shown to be identical for receivers with known states that are using either TOA or TDOA to localize multiple transmitters. In [23], the same conclusion was found for single emitter localization and was shown to be independent of the TDOA reference selection when the receivers were *stationary* and *time-synchronized*, with the measurement noise being independent and identically-distributed. These conclusions do

not extend to the CoRSLAM framework studied in this paper due to three reasons. The first pertains to the nature of radio SLAM, which is the unavailability of the SOPs' states that are simultaneously estimated with the AVs' states. The second arises because the AV-mounted receivers' and SOPs' clocks are practically unsynchronized. The third is because the measurement noise can not be assumed to be independent and identically-distributed.

The remainder of this paper is organized as follows. Section II describes the dynamics model of the SOPs and navigating AVs as well as the receivers' measurement model. Section III describes the TOA and TDOA information fusion strategies. Section IV compares the estimation performance of each strategy. Section V presents experimental results of collaborating UAVs using cellular signals to aid their INSs. Concluding remarks are given in Section VI.

II. Model Description

A. SOP Dynamics Model

Each SOP will be assumed to emanate from a spatially-stationary terrestrial transmitter, and its state vector will consist of its three-dimensional (3-D) position states $\boldsymbol{r}_{\mathrm{sop}_m} \triangleq \left[x_{\mathrm{sop}_m}, y_{\mathrm{sop}_m}, z_{\mathrm{sop}_m} \right]^\mathsf{T}$ and clock error states $\boldsymbol{x}_{\mathrm{clk,sop}_m} \triangleq \left[c\delta t_{\mathrm{sop}_m}, c\dot{\delta} t_{\mathrm{sop}_m} \right]^\mathsf{T}$, where c is the speed of light, $\delta t_{\mathrm{sop}_m}$ is the clock bias, $\dot{\delta} t_{\mathrm{sop}_m}$ is the clock drift, $m = 1, \ldots, M$, and M is the total number of SOPs.

The SOP's discretized dynamics are given by

$$\boldsymbol{x}_{\mathrm{sop}_m}(k+1) = \mathbf{F}_{\mathrm{sop}}\, \boldsymbol{x}_{\mathrm{sop}_m}(k) + \boldsymbol{w}_{\mathrm{sop}_m}(k), \quad k = 1, 2, \ldots,$$

$$\mathbf{F}_{\mathrm{sop}} = \begin{bmatrix} \mathbf{I}_{3\times 3} & \mathbf{0}_{3\times 2} \\ \mathbf{0}_{2\times 3} & \mathbf{F}_{\mathrm{clk}} \end{bmatrix}, \qquad \mathbf{F}_{\mathrm{clk}} = \begin{bmatrix} 1 & T \\ 0 & 1 \end{bmatrix}, \qquad (1)$$

where $\boldsymbol{x}_{\mathrm{sop}_m} = \left[\boldsymbol{r}_{\mathrm{sop}_m}^\mathsf{T}, \boldsymbol{x}_{\mathrm{clk,sop}_m}^\mathsf{T} \right]^\mathsf{T}$, $\boldsymbol{w}_{\mathrm{sop}_m}$ is the process noise, which is modeled as a discrete-time (DT) zero-mean white noise sequence with covariance $\mathbf{Q}_{\mathrm{sop}_m} = \mathrm{diag}\left[\mathbf{0}_{3\times 3}, c^2 \mathbf{Q}_{\mathrm{clk,sop}_m} \right]$, and

$$\mathbf{Q}_{\mathrm{clk,sop}_m} = \begin{bmatrix} S_{w_{\delta t_{\mathrm{sop},m}}} T + S_{w_{\dot{\delta} t_{\mathrm{sop},m}}} \frac{T^3}{3} & S_{w_{\dot{\delta} t_{\mathrm{sop},m}}} \frac{T^2}{2} \\ S_{w_{\dot{\delta} t_{\mathrm{sop},m}}} \frac{T^2}{2} & S_{w_{\dot{\delta} t_{\mathrm{sop},m}}} T \end{bmatrix},$$

where T is the constant sampling interval. The terms $S_{w_{\delta t_{\mathrm{sop},m}}}$ and $S_{w_{\dot{\delta} t_{\mathrm{sop},m}}}$ are the clock bias and drift process noise power spectra, respectively, which can be related to the power-law coefficients, $\left\{ h_{\alpha,\mathrm{sop}_m} \right\}_{\alpha=-2}^2$, which have been shown through laboratory experiments to characterize the power spectral density of the fractional frequency deviation of an oscillator from nominal frequency according to $S_{\delta t_{\mathrm{sop}_m}} \approx \frac{h_{0,\mathrm{sop}_m}}{2}$ and $S_{\dot{\delta} t_{\mathrm{sop}_m}} \approx 2\pi^2 h_{-2,\mathrm{sop}_m}$ [24].

B. Vehicle Dynamics Model

The nth AV state vector is $\boldsymbol{x}_{r_n} = \left[\boldsymbol{x}_{B_n}^\mathsf{T}, \boldsymbol{x}_{\mathrm{clk},r_n}^\mathsf{T} \right]^\mathsf{T}$, where $\boldsymbol{x}_{B_n}$ is the INS's state vector, $\boldsymbol{x}_{\mathrm{clk},r_n}$ is the AV-mounted receiver's clock state vector, $n = 1, \ldots, N$, and N is the total number of AVs.

The INS 16-state vector is

$$\boldsymbol{x}_{B_n} = \left[{}_G^B \boldsymbol{q}_n^\mathsf{T}, \quad \boldsymbol{r}_{r_n}^\mathsf{T}, \quad \boldsymbol{v}_{r_n}^\mathsf{T}, \quad \boldsymbol{b}_{g_n}^\mathsf{T}, \quad \boldsymbol{b}_{a_n}^\mathsf{T} \right]^\mathsf{T},$$

where $\boldsymbol{r}_{r_n}$ and $\boldsymbol{v}_{r_n}$ are the 3-D position and velocity, respectively, of the body frame expressed in a global frame, e.g., the Earth-centered Earth-fixed (ECEF) frame; $\boldsymbol{b}_{g_n}$ and $\boldsymbol{b}_{a_n}$ are the gyroscope and accelerometer biases, respectively; and ${}_G^B \boldsymbol{q}_n$ is the 4-D unit quaternion vector, which represents the orientation of the body frame with respect to a global frame [25].

1) Receiver Clock State Dynamics: The nth AV-mounted receiver's clock states will evolve according to

$$\boldsymbol{x}_{\mathrm{clk},r_n}(k+1) = \mathbf{F}_{\mathrm{clk}} \boldsymbol{x}_{\mathrm{clk},r_n}(k) + \boldsymbol{w}_{\mathrm{clk},r_n}(k), \qquad (2)$$

where $\boldsymbol{w}_{\mathrm{clk},r_n}$ is the process noise vector, which is modeled as a DT zero-mean white noise sequence with covariance $\mathbf{Q}_{\mathrm{clk},r_n}$, which has an identical form to $\mathbf{Q}_{\mathrm{clk,sop}_m}$, except that $S_{w_{\delta t_{\mathrm{sop},m}}}$ and $S_{w_{\dot{\delta} t_{\mathrm{sop},m}}}$ are now replaced with receiver-specific spectra $S_{w_{\delta t_{r,n}}}$ and $S_{w_{\dot{\delta} t_{r,n}}}$, respectively.

2) INS State Kinematics: The INS states will evolve in time according to

$$\boldsymbol{x}_{B_n}(k+1) = \boldsymbol{f}_{B_n}\left[\boldsymbol{x}_{B_n}(k), {}^B\boldsymbol{\omega}_n(k), {}^G\boldsymbol{a}_n(k) \right],$$

where $\boldsymbol{f}_{B_n}$ is a vector-valued function of standard kinematic equations, which are driven by the 3-D rotational rate vector ${}^B\boldsymbol{\omega}_n$ in the body frame and the 3-D acceleration of the IMU ${}^G\boldsymbol{a}_n$ in the global frame [26].

3) IMU Measurement Model: The IMU on the nth AV contains a triad-gyroscope and a triad-accelerometer, which produce measurements ${}^n\boldsymbol{z}_{\mathrm{imu}} \triangleq \left[{}^n\boldsymbol{\omega}_{\mathrm{imu}}^\mathsf{T}, {}^n\boldsymbol{a}_{\mathrm{imu}}^\mathsf{T} \right]^\mathsf{T}$ of the angular rate and specific force, which are modeled as

$$ {}^n\boldsymbol{\omega}_{\mathrm{imu}} = {}^B\boldsymbol{\omega}_n + \boldsymbol{b}_{g_n} + \boldsymbol{n}_{g_n} \qquad (3)$$

$$ {}^n\boldsymbol{a}_{\mathrm{imu}} = \mathbf{R}\left[{}_G^{B_k} \boldsymbol{q}_n \right] \left({}^G\boldsymbol{a}_n - {}^G\boldsymbol{g}_n \right) + \boldsymbol{b}_{a_n} + \boldsymbol{n}_{a_n}, \qquad (4)$$

where ${}_G^{B_k} \boldsymbol{q}_n$ represents the orientation of the body frame in a global frame at time-step k, $\mathbf{R}\left[\boldsymbol{q}_n\right]$ is the equivalent rotation matrix of $\boldsymbol{q}_n$, ${}^G\boldsymbol{g}_n$ is the acceleration due to gravity of the nth AV in the global frame, and $\boldsymbol{n}_{g_n}$ and $\boldsymbol{n}_{a_n}$ are measurement noise vectors, which are modeled as zero-mean white noise sequences with covariances $\sigma_{g_n}^2 \mathbf{I}_{3\times 3}$ and $\sigma_{a_n}^2 \mathbf{I}_{3\times 3}$, respectively.

C. Pseudorange Measurement Model

The pseudorange measurements made by the nth receiver on the mth SOP, after discretization and mild approximations discussed in [17], are modeled as

$$ {}^n z_{\mathrm{sop}_m}(j) = \| \boldsymbol{r}_{r_n}(j) - \boldsymbol{r}_{\mathrm{sop}_m} \|_2 + c \cdot \left[\delta t_{r_n}(j) - \delta t_{\mathrm{sop}_m}(j) \right] + {}^n v_{\mathrm{sop}_m}(j), \qquad (5)$$

where ${}^n v_{\mathrm{sop}_m}$ is the measurement noise, which is modeled as a DT zero-mean white Gaussian sequence with variance ${}^n\sigma_{\mathrm{sop}_m}^2$. The pseudorange measurement made by the nth receiver on

the lth GNSS SV, after compensating for ionospheric and tropospheric delays, is related to the receiver states by

$$\begin{aligned}
{}^{n}z_{\text{sv}_l}(j) = &\|\boldsymbol{r}_{r_n}(j) - \boldsymbol{r}_{\text{sv}_l}(j)\|_2 \\
&+ c \cdot [\delta t_{r_n}(j) - \delta t_{\text{sv}_l}(j)] + {}^{n}v_{\text{sv}_l}(j), \quad (6)
\end{aligned}$$

where ${}^{n}z_{\text{sv}_l} \triangleq {}^{n}z'_{\text{sv}_l} - c\delta t_{\text{iono}} - c\delta t_{\text{tropo}}$, δt_{iono} and δt_{tropo} are the ionospheric and tropospheric delays, respectively; ${}^{n}z'_{\text{sv}_l}$ is the uncorrected pseudorange; ${}^{n}v_{\text{sv}_l}$ is the measurement noise, which is modeled as a DT zero-mean white Gaussian sequence with variance ${}^{n}\sigma^2_{\text{sv}_l}$; and $l = 1, \dots, L$, where L is the total number of GNSS SVs.

III. Collaborative Radio SLAM Framework and Fusion Strategies

In this section, a distributed extended Kalman filter (EKF)-based CoRSLAM framework that fuses either TOA or TDOA measurements from SOPs is presented and described in detail. The EKF time and measurement update equations are provided for each fusion strategy. This framework operates in one of three modes: (1) a mapping mode when four or more GNSS SVs are available ($L \geq 4$), (2) a partial CoRSLAM mode when one to three GNSS SVs are available ($1 \leq L \leq 3$), and (3) a CoRSLAM mode when GNSS SVs are unavailable ($L = 0$). The partial CoRSLAM mode is analogous to a partial INS coasting mode that a traditional tightly-coupled GNSS-aided INS operates in when at least one (but less than four) GNSS SVs are available.

A. Distributed CoRSLAM Framework

In a CoRSLAM framework, the states of the SOPs are continuously estimated along with the states of the AVs. This can be achieved through an EKF with state vector

$$\boldsymbol{x} \triangleq \left[\boldsymbol{x}^{\mathsf{T}}_{r_1}, \dots, \boldsymbol{x}^{\mathsf{T}}_{r_N}, \boldsymbol{x}^{\mathsf{T}}_{\text{sop}_1}, \dots, \boldsymbol{x}^{\mathsf{T}}_{\text{sop}_M} \right]^{\mathsf{T}}.$$

To estimate the components of this vector, a distributed CoRSLAM framework in which AVs fuse information via a collaborative, tightly-coupled, SOP-aided INS framework is employed. A high-level diagram of this framework is illustrated in Fig. 1.

In traditional distributed approaches, each AV monitors a subset of the entire state vector, employing covariance intersection (or one of its variants) to fuse estimates with unknown inter-vehicle correlations and consensus algorithms when a fully connected network is not always available. In contrast, the approach of the framework in Fig. 1 is for each AV to monitor the entire state vector, but to distribute the INSs (the EKF prediction step) among the AVs and to optimize what information is shared and how often it is transmitted for aiding corrections. With the appropriate selection and transmission scheme of $\boldsymbol{\Lambda}_n$, identical estimates to a centralized approach are produced.

In the following sections, the TOA and TDOA information fusion strategies are described and compared. Both strategies have a common prediction (time update) step, which uses the
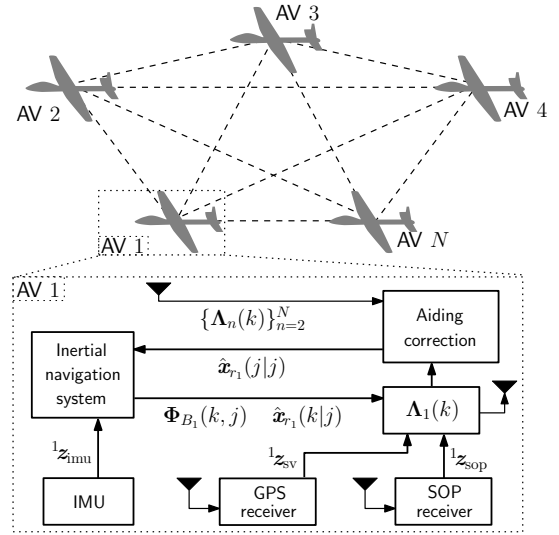

Fig. 1. Distributed SOP-aided INS framework. All N AVs maintain their own INSs. Each AV transmits a packet $\boldsymbol{\Lambda}_n(k)$ containing required information for each AV to produce an INS aiding correction.

on-board INS of each vehicle. Both strategies use GNSS pseudoranges as TOA measurements if they are available during the correction (measurement update) step. The distinction between these strategies is in how the SOP pseudoranges are fused to aid the AVs' on-board INSs: either TOA or TDOA with reference to selected SOPs.

B. Prediction

The EKF prediction produces $\hat{\boldsymbol{x}}(k|j) \triangleq \mathbb{E}[\boldsymbol{x}(k)|\boldsymbol{Z}^j]$ of $\boldsymbol{x}(k)$, where $\mathbb{E}[\cdot|\cdot]$ is the conditional expectation operator, $\boldsymbol{Z}^j \triangleq \{\boldsymbol{z}(i)\}^j_{i=1}$, $\boldsymbol{z}$ is a vector of INS-aiding measurements, $k \geq j$, and j is the last time-step an INS-aiding measurement was available. Between aiding updates, the INS on-board the nth AV integrates ${}^{n}\boldsymbol{z}_{\text{imu}}$ to produce a prediction of $\boldsymbol{x}_{B_n}$. The one-step prediction is given by

$$\hat{\boldsymbol{x}}_{B_n}(j+1|j) = \boldsymbol{f}_{B_n}\left[\hat{\boldsymbol{x}}_{B_n}(j|j), {}^{n}\boldsymbol{z}_{\text{imu}}(j+1) \right], \quad (7)$$

where the function $\boldsymbol{f}_{B_n}$ contains standard INS equations, which depend on the navigation frame used, the mechanization type, and the INS error model used, which are described in [26], [27]. Assuming there are κ time-steps between aiding updates, the AV uses IMU data $\{{}^{n}\boldsymbol{z}_{\text{imu}}(i)\}^k_{i=j}$ to recursively solve (7) to produce $\hat{\boldsymbol{x}}_{B_n}(k|j)$, where $k \equiv j+\kappa$. The receiver's κ-step clock state prediction follows from (2) and is given by

$$\hat{\boldsymbol{x}}_{\text{clk},r_n}(k|j) = \mathbf{F}^{\kappa}_{\text{clk}} \hat{\boldsymbol{x}}_{\text{clk},r_n}(j|j).$$

Each receiver locally produces the SOPs' κ-step state prediction, which follows from (1) and is given by

$$\hat{\boldsymbol{x}}_{\text{sop}_m}(k|j) = \mathbf{F}^{\kappa}_{\text{sop}} \hat{\boldsymbol{x}}_{\text{sop}_m}(j|j), \qquad m = 1, \dots, M.$$

The corresponding κ-step prediction error covariance is given by

$$\mathbf{P}_{\boldsymbol{x}}(k|j) = \mathbf{F}(k,j)\mathbf{P}_{\boldsymbol{x}}(j|j)\mathbf{F}^{\mathsf{T}}(k,j) + \mathbf{Q}^{+}(k,j), \quad (8)$$

$$\mathbf{F}(k,j) \triangleq \text{diag}\left[\mathbf{F}_{r_1}(k,j), \dots, \mathbf{F}_{r_N}(k,j), \mathbf{F}^{\kappa}_{\text{sop}}, \dots, \mathbf{F}^{\kappa}_{\text{sop}} \right],$$

$$\mathbf{F}_{r_n}(k,j) \triangleq \operatorname{diag}\left[\mathbf{\Phi}_{B_n}(k,j),\ \mathbf{F}_{\mathrm{clk}}^{\kappa}\right], \quad \mathbf{\Phi}_{B_n}(k,j) \triangleq \prod_{i=j}^{k} \mathbf{\Phi}_{B_n}(i),$$

where $\mathbf{\Phi}_{B_n}(i)$ is the Jacobian of $\boldsymbol{f}_{B_n}$ evaluated at $\hat{\boldsymbol{x}}_{B_n}(i|j)$. The matrix $\mathbf{Q}^{+}(k,j)$ is the propagated process noise covariance, which has the form

$$\mathbf{Q}^{+}(k,j) \triangleq \operatorname{diag}\big[\mathbf{Q}_{r_1}^{+}(k,j), \ldots, \mathbf{Q}_{r_N}^{+}(k,j),$$
$$\mathbf{Q}_{\mathrm{sop}_1}^{+}(k,j), \ldots, \mathbf{Q}_{\mathrm{sop}_M}^{+}(k,j)\big],$$

$$\mathbf{Q}_{r_n}^{+}(k,j) \triangleq \sum_{i=j}^{k} \mathbf{F}_{r_n}(i,j)\mathbf{Q}_{r_n}(i)\mathbf{F}_{r_n}^{\mathsf{T}}(i,j),$$

$$\mathbf{Q}_{\mathrm{sop}_m}^{+}(k,j) \triangleq \sum_{i=j}^{k} \mathbf{F}_{\mathrm{sop}}^{(i-j)}\mathbf{Q}_{\mathrm{sop}_m}[\mathbf{F}_{\mathrm{sop}}^{\mathsf{T}}]^{(i-j)},$$

where $\mathbf{Q}_{r_n}(i) \triangleq \operatorname{diag}\left[\mathbf{Q}_{\mathrm{d},B_n}(i),\ c^2\mathbf{Q}_{\mathrm{clk},r_n}\right]$ and $\mathbf{Q}_{\mathrm{d},B_n}$ is the nth AV's DT linearized INS process noise covariance, whose structure is dependent on the gyroscope's and accelerometer's error models used and is described in [26], [27].

C. Vehicle-to-Vehicle Communication

To produce the prediction error covariance (8) at each vehicle, the matrices $\{\mathbf{\Phi}_{B_n}(k,j)\}_{n=1}^{N}$ must be available. The components of these matrices are a function of the INS data from each respective AV. IMU data rates are typically between 100 Hz to 400 Hz, making the transmission of raw accelerometer and gyroscope data undesirable for several reasons: (i) large communication bandwidth requirement, (ii) packet drops due to lossy communication channels, and (iii) access to the raw IMU data may not be available. To address these issues, instead of transmitting raw IMU data, a packet $\mathbf{\Lambda}_n$ is broadcasted by the nth AV at the fixed rate of measurement epochs, which is given by

$$\mathbf{\Lambda}_n(k) \triangleq \left\{\hat{\boldsymbol{x}}_{B_n}(k|j),\ \mathbf{\Phi}_{B_n}(k,j),\ {}^{n}\boldsymbol{z}_{\mathrm{sv}}(k),\ {}^{n}\boldsymbol{z}_{\mathrm{sop}}(k)\right\}, \quad (9)$$

where ${}^{n}\boldsymbol{z}_{\mathrm{sv}}$ and ${}^{n}\boldsymbol{z}_{\mathrm{sop}}$ are GNSS and SOP pseudoranges, respectively, which are discussed further for each strategy in the following two subsections. The transmission of $\mathbf{\Lambda}_n$ has been shown to require significantly less communication rate and its performance was robust to moderate probability of packet loss [28]. Assuming a fully-connected graph, as in Fig. 1, the packets $\{\mathbf{\Lambda}_n(k)\}_{n=1}^{N}$ contain all relevant information required for each AV to compute the EKF update and the corresponding corrected estimation error covariance.

In the following two subsections, the correction equations are developed for two information fusion strategies: (1) TOA and (2) TDOA with SOP referencing.

D. TOA Information Fusion Strategy

In this subsection, the EKF-based CoRSLAM measurement update for fusing TOA measurements from SOPs is described. Specifically, the correction to the estimation error $\tilde{\boldsymbol{x}}(k|k)$ is provided, since it will be compared with the estimation error of the TDOA fusion strategy, denoted $\tilde{\bar{\boldsymbol{x}}}(k|k)$, in Section IV.

The EKF measurement update will correct the AVs' INS and clock errors given the measurement vector

$$\boldsymbol{z} \triangleq \left[\boldsymbol{z}_{\mathrm{sv}}^{\mathsf{T}},\ \boldsymbol{z}_{\mathrm{sop}}^{\mathsf{T}}\right]^{\mathsf{T}}, \quad (10)$$

$$\boldsymbol{z}_{\mathrm{sv}} \triangleq \left[{}^{1}\boldsymbol{z}_{\mathrm{sv}}^{\mathsf{T}}, \ldots, {}^{N}\boldsymbol{z}_{\mathrm{sv}}^{\mathsf{T}}\right]^{\mathsf{T}}, \quad \boldsymbol{z}_{\mathrm{sop}} \triangleq \left[{}^{1}\boldsymbol{z}_{\mathrm{sop}}^{\mathsf{T}}, \ldots, {}^{N}\boldsymbol{z}_{\mathrm{sop}}^{\mathsf{T}}\right]^{\mathsf{T}},$$

$${}^{n}\boldsymbol{z}_{\mathrm{sv}} = \left[{}^{n}z_{\mathrm{sv}_1}, \ldots, {}^{n}z_{\mathrm{sv}_L}\right]^{\mathsf{T}}, \quad {}^{n}\boldsymbol{z}_{\mathrm{sop}} = \left[{}^{n}z_{\mathrm{sop}_1}, \ldots, {}^{n}z_{\mathrm{sop}_M}\right]^{\mathsf{T}}.$$

The correction equations are described next for: (1) mapping ($L \geq 4$) and partial CoRSLAM mode ($1 \leq L \leq 3$) and (2) CoRSLAM mode ($L = 0$).

1) Correction Equations for Mapping and Partial CoRSLAM: Given a prediction error $\tilde{\boldsymbol{x}}(k|j)$, the error correction and corresponding corrected error covariance are given by

$$\tilde{\boldsymbol{x}}(k|k) = \tilde{\boldsymbol{x}}(k|j) - \mathbf{L}(k)\mathbf{S}^{-1}(k)\boldsymbol{\nu}(k),$$
$$\mathbf{P}_{\boldsymbol{x}}(k|k) = \mathbf{P}_{\boldsymbol{x}}(k|j) - \mathbf{L}(k)\mathbf{S}^{-1}(k)\mathbf{L}^{\mathsf{T}}(k), \quad (11)$$
$$\mathbf{L}(k) \triangleq \mathbf{P}_{\boldsymbol{x}}(k|j)\mathbf{H}^{\mathsf{T}}(k), \quad (12)$$
$$\mathbf{S}(k) \triangleq \mathbf{H}(k)\mathbf{L}(k) + \mathbf{R}(k), \quad (13)$$
$$\boldsymbol{\nu}(k) \triangleq \boldsymbol{z}(k) - \hat{\boldsymbol{z}}(k|j), \quad (14)$$

where $\hat{\boldsymbol{z}}(k|j)$ is a vector containing the predicted GNSS pseudoranges and the predicted SOP TOA measurement set. The matrix $\mathbf{H}$ is the measurement Jacobian and has the form

$$\mathbf{H} = \begin{bmatrix} \mathbf{H}_{\mathrm{sv},r} & \mathbf{0}_{NL \times 5M} \\ \mathbf{H}_{\mathrm{sop},r} & \mathbf{H}_{\mathrm{sop}} \end{bmatrix}, \quad \mathbf{H}_{\mathrm{sv},r} \triangleq \operatorname{diag}\left[{}^{1}\mathbf{H}_{\mathrm{sv},r}, \ldots, {}^{N}\mathbf{H}_{\mathrm{sv},r}\right],$$

$${}^{n}\mathbf{H}_{\mathrm{sv},r} = \begin{bmatrix} \mathbf{0}_{1\times 3} & {}^{n}\hat{\mathbf{1}}_{\mathrm{sv}_1}^{\mathsf{T}} & \mathbf{0}_{1\times 9} & \boldsymbol{h}_{\mathrm{clk}}^{\mathsf{T}} \\ \vdots & \vdots & \vdots & \vdots \\ \mathbf{0}_{1\times 3} & {}^{n}\hat{\mathbf{1}}_{\mathrm{sv}_L}^{\mathsf{T}} & \mathbf{0}_{1\times 9} & \boldsymbol{h}_{\mathrm{clk}}^{\mathsf{T}} \end{bmatrix},$$
$$\mathbf{H}_{\mathrm{sop},r} \triangleq \operatorname{diag}\left[{}^{1}\mathbf{H}_{\mathrm{sop},r}, \ldots, {}^{N}\mathbf{H}_{\mathrm{sop},r}\right],$$

where ${}^{n}\mathbf{H}_{\mathrm{sop},r}$ has the same structure as ${}^{n}\mathbf{H}_{\mathrm{sv},r}$, except ${}^{n}\hat{\mathbf{1}}_{\mathrm{sv}_l}^{\mathsf{T}}$ is replaced with ${}^{n}\hat{\mathbf{1}}_{\mathrm{sop}_m}^{\mathsf{T}}$,

$$\mathbf{H}_{\mathrm{sop}} \triangleq \left[{}^{1}\mathbf{H}_{\mathrm{sop}}^{\mathsf{T}}, \ldots, {}^{N}\mathbf{H}_{\mathrm{sop}}^{\mathsf{T}}\right]^{\mathsf{T}},$$
$${}^{n}\mathbf{H}_{\mathrm{sop}} = \operatorname{diag}\left[{}^{n}\mathbf{H}_{\mathrm{sop}_1}, \ldots, {}^{n}\mathbf{H}_{\mathrm{sop}_M}\right],$$
$${}^{n}\hat{\mathbf{1}}_{\mathrm{sv}_l} \triangleq \frac{\hat{\boldsymbol{r}}_{r_n} - \boldsymbol{r}_{\mathrm{sv}_l}}{\|\hat{\boldsymbol{r}}_{r_n} - \boldsymbol{r}_{\mathrm{sv}_l}\|}, \quad {}^{n}\hat{\mathbf{1}}_{\mathrm{sop}_m} \triangleq \frac{\hat{\boldsymbol{r}}_{r_n} - \hat{\boldsymbol{r}}_{\mathrm{sop}_m}}{\|\hat{\boldsymbol{r}}_{r_n} - \hat{\boldsymbol{r}}_{\mathrm{sop}_m}\|},$$
$${}^{n}\mathbf{H}_{\mathrm{sop}_m} \triangleq \left[-{}^{n}\hat{\mathbf{1}}_{\mathrm{sop}_m}^{\mathsf{T}},\ -\boldsymbol{h}_{\mathrm{clk}}^{\mathsf{T}}\right], \quad \boldsymbol{h}_{\mathrm{clk}} \triangleq [1, 0]^{\mathsf{T}},$$

and $\mathbf{R}$ is the measurement noise covariance. Note that $\mathbf{R}$ is not necessarily diagonal, since there are no assumptions made on the measurement noise statistics, except that $\mathbf{R} \succ \mathbf{0}$.

2) Correction Equations for CoRSLAM: The CoRSLAM mode is similar to the mapping and partial CoRSLAM modes, with the exception that GNSS SV pseudoranges are no longer available, i.e., $\boldsymbol{z} \equiv \boldsymbol{z}_{\mathrm{sop}}$. The state and covariance correction are identical, except that the Jacobian is adjusted to account for GNSS SV pseudoranges no longer being available, specifically

$$\mathbf{H} \equiv [\mathbf{H}_{\mathrm{sop},r},\ \mathbf{H}_{\mathrm{sop}}]. \quad (15)$$

E. TDOA with SOP Referencing Information Fusion Strategy

In this information fusion strategy, TDOA measurements are computed at each receiver by differencing the drawn pseudo-ranges with a selected reference SOP. The produced estimation error and covariance of $\boldsymbol{x}$ when TDOA measurements are used will be denoted $\tilde{\bar{\boldsymbol{x}}}$, and $\mathbf{P}_{\bar{\boldsymbol{x}}}$, respectively.

1) TDOA Measurements: Each receiver is free to select an arbitrary reference SOP, i.e., the SOP measurement set computed by the nth AV becomes

$$
\begin{aligned}
{}^{n}\bar{\boldsymbol{z}}_{\text{sop}}^{\mathsf{T}} &\triangleq \left[{}^{n}\bar{z}_{\text{sop}_1}, \ldots, {}^{n}\bar{z}_{\text{sop}_M}\right]^{\mathsf{T}}, \\
{}^{n}\bar{z}_{\text{sop}_m} &\triangleq {}^{n}z_{\text{sop}_m} - {}^{n}z_{\text{sop}_{\iota_n}} \\
&= \|\boldsymbol{r}_{r_n}(j) - \boldsymbol{r}_{\text{sop}_m}\|_2 - \|\boldsymbol{r}_{r_n}(j) - \boldsymbol{r}_{\text{sop}_{\iota_n}}\|_2 \\
&\quad + c \cdot [\delta t_{\text{sop}_m}(j) - \delta t_{\text{sop}_{\iota_n}}(j)] \\
&\quad + {}^{n}v_{\text{sop}_m}(j) - {}^{n}v_{\text{sop}_{\iota_n}}(j),
\end{aligned}
\tag{16}
$$

where ι_n is the reference SOP number used by the nth AV and $m \in \{1, \ldots, M\} \backslash \iota_n$. Each receiver replaces the SOP TOA measurements $\boldsymbol{z}_{\text{sop}}$ with the SOP TDOA measurements $\bar{\boldsymbol{z}}_{\text{sop}}$ in the transmitted packet (9). Note that since the SOP transmitters are not synchronized, the TDOA measurements (16) are parameterized by the clock biases of both transmitters; therefore, both of these biases must be estimated. This differs from traditional TDOA-based localization approaches that assume synchronized transmitters, which allow for these biases to cancel and to be removed from the estimator.

The measurement set available to each receiver in the TDOA fusion strategy may be written in terms of the measurement set (10) of the TOA fusion strategy as

$$
\bar{\boldsymbol{z}} \triangleq \begin{bmatrix} \boldsymbol{z}_{\text{sv}} \\ \bar{\boldsymbol{z}}_{\text{sop}} \end{bmatrix} = \begin{bmatrix} \mathbf{I}_{NL \times NL} & \mathbf{0}_{NL \times NM} \\ \mathbf{0}_{NM \times NL} & \mathbf{T} \end{bmatrix} \begin{bmatrix} \boldsymbol{z}_{\text{sv}} \\ \boldsymbol{z}_{\text{sop}} \end{bmatrix} \triangleq \boldsymbol{\Xi}\boldsymbol{z} \tag{17}
$$

where $\mathbf{I}_{NL \times NL}$ is an $NL \times NL$ identity matrix and $\mathbf{T}$ is the difference operator matrix that maps $\boldsymbol{z}_{\text{sop}}$ to $\bar{\boldsymbol{z}}_{\text{sop}}$, which has the form

$$
\mathbf{T} = \text{diag}\left[\mathbf{T}_{\iota_1}, \ldots \mathbf{T}_{\iota_N}\right], \tag{18}
$$

$$
\mathbf{T}_{\iota_n} = \begin{bmatrix} 1 & \cdots & 0 & -1 & 0 & \cdots & 0 \\ \vdots & \ddots & \vdots & \vdots & \vdots & \ddots & \vdots \\ 0 & \cdots & 1 & -1 & 0 & \cdots & 0 \\ 0 & \cdots & 0 & -1 & 1 & \cdots & 0 \\ \vdots & \ddots & \vdots & \vdots & \vdots & \ddots & \vdots \\ 0 & \cdots & 0 & -1 & 0 & \cdots & 1 \end{bmatrix}, \tag{19}
$$

where the column of "−1" resides in column ι_n. The prediction error covariance $\mathbf{P}_{\bar{\boldsymbol{x}}}(k|j)$ is dependent only on the IMU data; therefore, has the same form as (8). The correction equations are summarized next.

2) Correction Equations for Mapping and Partial CoRSLAM: The following equations are valid for both $L \geq 4$ and $1 \leq L \leq 3$:

$$
\tilde{\bar{\boldsymbol{x}}}(k|k) = \tilde{\bar{\boldsymbol{x}}}(k|j) - \bar{\mathbf{L}}(k)\bar{\mathbf{S}}^{-1}\bar{\boldsymbol{\nu}}(k), \tag{20}
$$

$$
\mathbf{P}_{\bar{\boldsymbol{x}}}(k|k) = \mathbf{P}_{\bar{\boldsymbol{x}}}(k|j) - \bar{\mathbf{L}}(k)\bar{\mathbf{S}}^{-1}(k)\bar{\mathbf{L}}^{\mathsf{T}}(k), \tag{21}
$$

$$
\bar{\mathbf{L}}(k) \triangleq \mathbf{P}_{\bar{\boldsymbol{x}}}(k|j)\bar{\mathbf{H}}^{\mathsf{T}}(k) \tag{22}
$$

$$
\bar{\mathbf{S}}(k) \triangleq \bar{\mathbf{H}}(k)\bar{\mathbf{L}}(k) + \bar{\mathbf{R}}(k) \tag{23}
$$

$$
\bar{\boldsymbol{\nu}}(k) \triangleq \bar{\boldsymbol{z}}(k) - \hat{\bar{\boldsymbol{z}}}(k|j), \tag{24}
$$

where $\hat{\bar{\boldsymbol{z}}}(k|j)$ is the predicted GNSS pseudoranges and SOP TDOA measurement set and $\bar{\mathbf{H}}$ is the corresponding measurement Jacobian, which is related to $\mathbf{H}$ through

$$
\bar{\mathbf{H}} \triangleq \begin{bmatrix} \mathbf{I}_{NL \times NL} & \mathbf{0}_{NL \times NM} \\ \mathbf{0}_{NM \times NL} & \mathbf{T} \end{bmatrix} \begin{bmatrix} \mathbf{H}_{\text{sv},r} & \mathbf{0}_{NL \times 5M} \\ \mathbf{H}_{\text{sop},r} & \mathbf{H}_{\text{sop}} \end{bmatrix}.
$$

The measurement noise covariance is given by $\bar{\mathbf{R}} = \boldsymbol{\Xi}\mathbf{R}\boldsymbol{\Xi}^{\mathsf{T}}$.

3) Correction Equations for CoRSLAM: The CoRSLAM mode is similar to the mapping and partial CoRSLAM modes, with the exception that GNSS SV pseudoranges are no longer available, i.e., $\bar{\boldsymbol{z}} \equiv \bar{\boldsymbol{z}}_{\text{sop}}$. The state and covariance corrections are identical, except that the dimension of $\mathbf{I}_{NL \times NL}$ reduces to zero, modifying the measurement Jacobian to take the form

$$
\bar{\mathbf{H}} = \mathbf{T}\mathbf{H}, \tag{25}
$$

where $\mathbf{H}$ is the measurement Jacobian (15) from the TOA fusion strategy when $L = 0$.

IV. STRATEGY PERFORMANCE COMPARISON

In this section, the estimation performance of the two information fusion strategies presented in Section III are studied. First, it is shown that the TDOA estimation performance is invariant to the SOP reference selection. Then, it is shown that the TOA strategy yields less than or equal estimation error covariance corresponding to the AVs' positions than the TDOA strategy.

A. TDOA SOP Reference Selection

In this subsection, it is shown that the estimation error and error covariance are invariant to the choice of the SOP reference, which is summarized in Theorem IV.1.

Theorem IV.1. *Consider an environment comprising N receivers and M unknown SOPs with arbitrary: (i) receiver and SOP clock qualities (i.e., arbitrary $\{\mathbf{Q}_{\text{clk},r_n}\}_{n=1}^{N}$ and $\{\mathbf{Q}_{\text{clk},\text{sop}_m}\}_{m=1}^{M}$), (ii) geometric configurations, and (iii) measurement noise covariance (i.e., $\mathbf{R} \succ \mathbf{0}$, but not necessarily diagonal). The EKF-based CoRSLAM yields an estimation error and corresponding estimation error covariance that are invariant to each receiver's SOP reference selection.*

Proof. The proof will only consider the CoRSLAM mode ($L = 0$), i.e., $\bar{\boldsymbol{z}} \equiv \bar{\boldsymbol{z}}_{\text{sop}}$. The proof can be straightforwardly extended to the other modes ($1 \leq L \leq 3$ and $L \geq 4$). Given

$\tilde{\bar{x}}(k|j)$, the correction $\tilde{\bar{x}}(k|k)$ can be computed from (20). Substituting (25) into (22)-(24) gives

$$\bar{\mathbf{L}}(k) = \mathbf{P}_{\boldsymbol{x}}(k|j)\mathbf{H}^{\mathsf{T}}(k)\mathbf{T}^{\mathsf{T}}$$
$$= \mathbf{L}(k)\mathbf{T}^{\mathsf{T}}, \tag{26}$$
$$\bar{\mathbf{S}}(k) = \mathbf{T}\mathbf{H}(k)\mathbf{L}(k)\mathbf{T}^{\mathsf{T}} + \mathbf{T}\mathbf{R}(k)\mathbf{T}^{\mathsf{T}}$$
$$= \mathbf{T}\mathbf{S}(k)\mathbf{T}^{\mathsf{T}}, \tag{27}$$
$$\bar{\boldsymbol{\nu}}(k) = \mathbf{T}\boldsymbol{z}(k) - \mathbf{T}\hat{\boldsymbol{z}}(k|j)$$
$$= \mathbf{T}\boldsymbol{\nu}(k). \tag{28}$$

Substituting (26)-(28) into (20) yields

$$\tilde{\bar{x}}(k|k) = \tilde{\bar{x}}(k|j) - \mathbf{L}(k)\mathbf{T}^{\mathsf{T}}$$
$$\cdot [\mathbf{T}\mathbf{S}(k)\mathbf{T}^{\mathsf{T}}]^{-1}\mathbf{T}\boldsymbol{\nu}(k). \tag{29}$$

Recall that $\mathbf{T}$ is the difference operator, which computes the TDOA measurements when the nth receiver references the drawn pseudoranges with respect to an arbitrary SOP number ι_n and has the block diagonal structure (18).

Next, consider the block of $\mathbf{T}$ that corresponds to the nth receiver, which can be written as

$$\mathbf{T}_{\iota_n} = \mathbf{J}_{\iota_n} - \boldsymbol{v}\boldsymbol{e}_{\iota_n}^{\mathsf{T}}, \tag{30}$$

where $\mathbf{J}_{\iota_n} \in \mathbb{R}^{[(M-1)\times M]}$ is formed by removing the ι_n^{th} row from an identity matrix,

$$\boldsymbol{v} \triangleq [1, \ldots, 1]^{\mathsf{T}} \in \mathbb{R}^{(M-1)},$$

and $\boldsymbol{e}_{\iota_n}$ denotes the ι_n^{th} standard basis vector of appropriate dimension consisting of a 1 in the ι_n^{th} element and zeros elsewhere. From (30), it is easy to verify that $\mathbf{T}_{\iota_n} \in \mathbb{R}^{[(M-1)\times M]}$ is full row-rank and that $\mathbf{1} \triangleq [\boldsymbol{v}^{\mathsf{T}}, 1]^{\mathsf{T}}$ is a basis for the null space of $\mathbf{T}_{\iota_n}$; therefore,

$$\mathbf{0} = \mathbf{T}_{\iota_n}\mathbf{1} = \sum_{i=1}^{M} \mathbf{T}_{\iota_n}\boldsymbol{e}_i$$
$$\Rightarrow -\sum_{\substack{i=1 \\ i\neq q}}^{M} \boldsymbol{t}_{\iota_n,i} = \boldsymbol{t}_{\iota_n,q}, \quad \forall q \in [1,\ldots,M], \tag{31}$$

where $\boldsymbol{t}_{\iota_n,i} \triangleq \mathbf{T}_{\iota_n}\boldsymbol{e}_i$ and $\boldsymbol{t}_{\iota_n,q} \triangleq \mathbf{T}_{\iota_n}\boldsymbol{e}_q$ denote the ith and q^{th} column of $\mathbf{T}_{\iota_n}$, respectively. Partitioning $\mathbf{T}_{\iota_n}$ into columns yields

$$\mathbf{T}_{\iota_n} = [\boldsymbol{t}_{\iota_n,1}, \ldots, \boldsymbol{t}_{\iota_n,M}]$$
$$= [\mathbf{T}_{\iota_n,1:M-1}, \boldsymbol{t}_{\iota_n,M}], \tag{32}$$

where $\mathbf{T}_{\iota_n,1:M-1}$ denotes the matrix consisting of the columns $\boldsymbol{t}_{\iota_n,1}$ through $\boldsymbol{t}_{\iota_n,M-1}$. Substituting the left side of (31) for $q \equiv M$ into the last column of (32) gives

$$\mathbf{T}_{\iota_n} = \left[\mathbf{T}_{\iota_n,1:M-1}, -\sum_{i=1}^{M-1} \boldsymbol{t}_{\iota_n,i}\right]. \tag{33}$$

Next, consider the difference operator matrix

$$\mathbf{T}' = \text{diag}\left[\mathbf{T}_{\iota_1'}, \ldots \mathbf{T}_{\iota_N'}\right], \tag{34}$$

which forms the set of TDOA measurements when the nth receiver uses SOP ι_n' as its reference, where $\iota_n' \in [1,\ldots,M]$. Proceeding in a similar manner that was used to write $\mathbf{T}_{\iota_n}$ as (33), it is straight forward to show that $\mathbf{T}_{\iota_n'}$ can be written as

$$\mathbf{T}_{\iota_n'} = \left[\mathbf{T}_{\iota_n',1:M-1}, -\sum_{i=1}^{M-1} \boldsymbol{t}_{\iota_n',i}\right]. \tag{35}$$

Note that since $\mathbf{T}_{\iota_n}$ and $\mathbf{T}_{\iota_n'}$ are full row-rank, the matrices $\mathbf{T}_{\iota_n,1:M-1}$ and $\mathbf{T}_{\iota_n',1:M-1}$ are square and invertible; therefore, there exists a matrix $\mathbf{E}_n$, such that

$$\mathbf{T}_{\iota_n',1:M-1} = \mathbf{E}_n^{-1}\mathbf{T}_{\iota_n,1:M-1}. \tag{36}$$

From (36), the columns of $\mathbf{T}_{\iota_n',1:M-1}$ are related to the columns of $\mathbf{T}_{\iota_n,1:M-1}$ through

$$\boldsymbol{t}_{\iota_n',i} = \mathbf{E}_n^{-1}\boldsymbol{t}_{\iota_n,i}, \quad i = 1,\ldots,M-1. \tag{37}$$

Substituting the right side of (36) and (37) into the right side of (35) yields

$$\mathbf{T}_{\iota_n'} = \left[\mathbf{E}_n^{-1}\mathbf{T}_{\iota_n,1:M-1}, -\mathbf{E}_n^{-1}\sum_{i=1}^{M-1}\boldsymbol{t}_{\iota_n,i}\right]$$
$$= \mathbf{E}_n^{-1}\mathbf{T}_{\iota_n}. \tag{38}$$

The relationship between $\mathbf{T}'$ and $\mathbf{T}$ can be found by substituting (38) into (34) for $n = 1,\ldots,N$, which gives

$$\mathbf{T}' = \text{diag}\left[\mathbf{E}_1^{-1}\mathbf{T}_{\iota_1}, \ldots, \mathbf{E}_N^{-1}\mathbf{T}_{\iota_N}\right]$$
$$= \mathbf{E}^{-1}\mathbf{T}, \tag{39}$$

where $\mathbf{E}^{-1} \triangleq \text{diag}\left[\mathbf{E}_1^{-1}, \ldots, \mathbf{E}_N^{-1}\right]$. Solving (39) for $\mathbf{T}$ and substituting into (29) gives

$$\tilde{\bar{x}}(k|k) = \tilde{\bar{x}}(k|j) - \mathbf{L}(k)\mathbf{T}'^{\mathsf{T}}\mathbf{E}^{\mathsf{T}}$$
$$\cdot [\mathbf{E}\mathbf{T}'\mathbf{S}(k)\mathbf{T}'^{\mathsf{T}}\mathbf{E}^{\mathsf{T}}]^{-1}\mathbf{E}\mathbf{T}'\boldsymbol{\nu}(k)$$
$$= \tilde{\bar{x}}(k|j) - \mathbf{L}(k)\mathbf{T}'^{\mathsf{T}}\mathbf{E}^{\mathsf{T}}$$
$$\cdot \mathbf{E}^{-\mathsf{T}}[\mathbf{T}'\mathbf{S}(k)\mathbf{T}'^{\mathsf{T}}]^{-1}\mathbf{E}^{-1}\mathbf{E}\mathbf{T}'\boldsymbol{\nu}(k)$$
$$= \tilde{\bar{x}}'(k|k), \tag{40}$$

where $\tilde{\bar{x}}'(k|k)$ is the estimation error correction when the difference operator matrix $\mathbf{T}'$ is used. The last step in (40) follows from $\tilde{\bar{x}}(k|j) = \tilde{\bar{x}}'(k|j)$, since they only depend on IMU data, making (40) take the same form as (29), except that $\mathbf{T}$ is replaced with $\mathbf{T}'$.

Next, consider the EKF Riccati equation, which governs the time-evolution of the estimation error covariance

$$\mathbf{P}_{\bar{x}}(j+\kappa|j) = \mathbf{F}\big\{\mathbf{P}_{\bar{x}}(j|j-\kappa) - \mathbf{P}_{\bar{x}}(j|j-\kappa)\bar{\mathbf{H}}^{\mathsf{T}}(j)$$
$$\cdot \big[\bar{\mathbf{H}}(j)\mathbf{P}_{\bar{x}}(j|j-\kappa)\bar{\mathbf{H}}^{\mathsf{T}}(j) + \bar{\mathbf{R}}(j)\big]^{-1}$$
$$\cdot \bar{\mathbf{H}}(j)\mathbf{P}_{\bar{x}}(j|j-\kappa)\big\}\mathbf{F}^{\mathsf{T}} + \mathbf{Q}^{+}(j+\kappa,j),$$

where the time arguments $(j + \kappa, j)$ have been dropped from $\mathbf{F}$ to simplify the notation. Substituting (25) into $\bar{\mathbf{H}}$ and using the relationship found in (38) gives

$$
\begin{aligned}
\mathbf{P}_{\bar{\boldsymbol{x}}}&(j + \kappa | j) \\
&= \mathbf{F}\big\{ \mathbf{P}_{\bar{\boldsymbol{x}}}(j|j - \kappa) - \mathbf{P}_{\bar{\boldsymbol{x}}}(j|j - \kappa)\mathbf{H}^{\mathsf{T}}(j)\mathbf{T}^{\mathsf{T}} \\
&\quad \cdot \big[\mathbf{TH}(j)\mathbf{P}_{\bar{\boldsymbol{x}}}(j|j - \kappa)\mathbf{H}^{\mathsf{T}}(j)\mathbf{T}^{\mathsf{T}} + \mathbf{TR}(j)\mathbf{T}^{\mathsf{T}}\big]^{-1} \\
&\quad \cdot \mathbf{TH}(j)\mathbf{P}_{\bar{\boldsymbol{x}}}(j|j - \kappa)\big\}\mathbf{F}^{\mathsf{T}} + \mathbf{Q}^{+}(j + \kappa, j) \\
&= \mathbf{F}\big\{ \mathbf{P}_{\bar{\boldsymbol{x}}}(j|j - \kappa) - \mathbf{P}_{\bar{\boldsymbol{x}}}(j|j - \kappa)\mathbf{H}^{\mathsf{T}}(j)\mathbf{T}'^{\mathsf{T}}\mathbf{E}^{\mathsf{T}} \\
&\quad \cdot \mathbf{E}^{-\mathsf{T}}\big[\mathbf{T}'\mathbf{H}(j)\mathbf{P}_{\bar{\boldsymbol{x}}}(j|j - \kappa)\mathbf{H}^{\mathsf{T}}(j)\mathbf{T}'^{\mathsf{T}} + \mathbf{T}'\mathbf{R}(j)\mathbf{T}'^{\mathsf{T}}\big]^{-1}\mathbf{E}^{-1} \\
&\quad \cdot \mathbf{ET}'\mathbf{H}(j)\mathbf{P}_{\bar{\boldsymbol{x}}}(j|j - \kappa)\big\}\mathbf{F}^{\mathsf{T}} + \mathbf{Q}^{+}(j + \kappa, j) \\
&= \mathbf{P}_{\bar{\boldsymbol{x}}'}(j + \kappa | j),
\end{aligned}
$$

where $\mathbf{P}_{\bar{\boldsymbol{x}}'}(j + \kappa | j)$ is the prediction error covariance when the difference operator matrix $\mathbf{T}'$ is used. $\qquad \square$

B. TOA Versus TDOA

In this subsection, it is shown that fusing TOA measurements from unknown SOPs produces a less than or equal (in a positive semi-definite sense) position estimation error covariance matrix for each AV than fusing TDOA.

Theorem IV.2. *Consider an environment comprising N receivers and M unknown SOPs with arbitrary: (i) receiver and SOP clock qualities (i.e., arbitrary $\{\mathbf{Q}_{\mathrm{clk},r_n}\}_{n=1}^{N}$ and $\{\mathbf{Q}_{\mathrm{clk},\mathrm{sop}_m}\}_{m=1}^{M}$), (ii) geometric configurations, and (iii) measurement noise covariance (i.e., $\mathbf{R} \succ \mathbf{0}$, but not necessarily diagonal). The EKF-based CoRSLAM that fuses pseudoranges with a TOA fashion yields a less than or equal (in a positive semi-definite sense) position estimation error covariance for each of the AVs than a TDOA fashion.*

Proof. Define the correction (measurement update) estimation error covariance associated with the nth receiver's position for fusing TOA measurements at time-step k as

$$
\mathbf{P}_{\boldsymbol{r}_{r_n}}(k|k) \triangleq \boldsymbol{\Upsilon}_n \mathbf{P}_{\boldsymbol{x}}(k|k)\boldsymbol{\Upsilon}_n^{\mathsf{T}} \tag{41}
$$

and the correction (measurement update) estimation error covariance associated with the nth receiver's position for fusing TDOA measurements at time-step k as

$$
\mathbf{P}_{\bar{\boldsymbol{r}}_{r_n}}(k|k) \triangleq \boldsymbol{\Upsilon}_n \mathbf{P}_{\bar{\boldsymbol{x}}}(k|k)\boldsymbol{\Upsilon}_n^{\mathsf{T}}, \tag{42}
$$

where

$$
\boldsymbol{\Upsilon}_n \triangleq \big[\mathbf{0}_{3\times\gamma_{n,1}}, \mathbf{I}_{3\times3}, \mathbf{0}_{3\times\gamma_{n,2}}\big],
$$

$\gamma_{n,1} \triangleq 17n - 14$, and $\gamma_{n,2} \triangleq 17(N-n) + 5M - 11$. Substituting (11) and (21) into $\mathbf{P}_{\boldsymbol{x}}(k|k)$ and $\mathbf{P}_{\bar{\boldsymbol{x}}}(k|k)$ in (41) and (42), respectively, and differencing yields

$$
\begin{aligned}
\mathbf{P}_{\bar{\boldsymbol{r}}_{r_n}}&(k|k) - \mathbf{P}_{\boldsymbol{r}_{r_n}}(k|k) \\
&= \boldsymbol{\Upsilon}_n\big[\mathbf{L}(k)\mathbf{S}^{-1}(k)\mathbf{L}^{\mathsf{T}}(k) - \bar{\mathbf{L}}(k)\bar{\mathbf{S}}^{-1}(k)\bar{\mathbf{L}}^{\mathsf{T}}(k)\big]\boldsymbol{\Upsilon}_n^{\mathsf{T}}. \tag{43}
\end{aligned}
$$

Note that the prediction error covariances $\mathbf{P}_{\boldsymbol{x}}(k|j)$ and $\mathbf{P}_{\bar{\boldsymbol{x}}}(k|j)$ are only a function of the IMU data, making them independent of the information fusion type, i.e., $\mathbf{P}_{\boldsymbol{x}}(k|j) =$

$\mathbf{P}_{\bar{\boldsymbol{x}}}(k|j)$; therefore, they have canceled and did not appear in (43). Substituting (26) and (27) into (43) gives

$$
\begin{aligned}
\mathbf{P}_{\bar{\boldsymbol{r}}_{r_n}}&(k|k) - \mathbf{P}_{\boldsymbol{r}_{r_n}}(k|k) \\
&= \boldsymbol{\Upsilon}_n\big[\mathbf{L}(k)\mathbf{S}^{-1}(k)\mathbf{L}^{\mathsf{T}}(k) \\
&\quad - \mathbf{L}(k)\mathbf{T}^{\mathsf{T}}\big(\mathbf{TS}(k)\mathbf{T}^{\mathsf{T}}\big)^{-1}\mathbf{T}^{\mathsf{T}}\mathbf{L}^{\mathsf{T}}(k)\big]\boldsymbol{\Upsilon}_n^{\mathsf{T}} \\
&= \boldsymbol{\Upsilon}_n\mathbf{L}(k)\big[\mathbf{S}^{-1}(k) - \mathbf{T}\big(\mathbf{TS}(k)\mathbf{T}^{\mathsf{T}}\big)^{-1}\mathbf{T}^{\mathsf{T}}\big]\mathbf{L}^{\mathsf{T}}(k)\boldsymbol{\Upsilon}_n^{\mathsf{T}}. \tag{44}
\end{aligned}
$$

Define the matrices

$$
\begin{aligned}
\mathbf{A}(k) &\triangleq \mathbf{S}_c(k)\mathbf{T}^{\mathsf{T}} \in \mathbb{R}^{NM \times N(M-1)}, \tag{45} \\
\mathbf{B}_n(k) &\triangleq \boldsymbol{\Upsilon}_n\mathbf{L}(k)\mathbf{S}_c^{-1}(k) \in \mathbb{R}^{3 \times NM}, \quad n = 1,\ldots,N, \tag{46}
\end{aligned}
$$

where $\mathbf{S}_c$ is the Cholesky decomposition of $\mathbf{S}$, i.e., $\mathbf{S} = \mathbf{S}_c\mathbf{S}_c^{\mathsf{T}}$. Since $\mathbf{S}$ is symmetric positive definite, $\mathbf{S}_c$ is unique and invertible. Substituting (45) and (46) into (44) yields

$$
\begin{aligned}
\mathbf{P}_{\bar{\boldsymbol{r}}_{r_n}}&(k|k) - \mathbf{P}_{\boldsymbol{r}_{r_n}}(k|k) \\
&= \mathbf{B}_n(k)\big[\mathbf{I}_{NM \times NM} - \mathbf{A}(k)\big[\mathbf{A}^{\mathsf{T}}(k)\mathbf{A}(k)\big]^{-1}\mathbf{A}^{\mathsf{T}}(k)\big]\mathbf{B}_n^{\mathsf{T}}(k), \tag{47}
\end{aligned}
$$

where $\mathbf{I}_{NM \times NM}$ is a $NM \times NM$ identity matrix. Define the matrix

$$
\boldsymbol{\Omega}(k) \triangleq \mathbf{A}(k)\big[\mathbf{A}^{\mathsf{T}}(k)\mathbf{A}(k)\big]^{-1}\mathbf{A}^{\mathsf{T}}(k). \tag{48}
$$

Substituting (48) into (47) gives

$$
\mathbf{P}_{\bar{\boldsymbol{r}}_{r_n}}(k|k) - \mathbf{P}_{\boldsymbol{r}_{r_n}}(k|k) = \mathbf{B}_n(k)\mathbf{M}(k)\mathbf{B}_n^{\mathsf{T}}(k), \tag{49}
$$

where $\mathbf{M}(k) \triangleq \mathbf{I}_{NM \times NM} - \boldsymbol{\Omega}(k)$. Note that,

(i) The matrix $\boldsymbol{\Omega} \in \mathbb{R}^{NM \times NM}$ is an orthogonal projection matrix, since it satisfies $\boldsymbol{\Omega}^2 = \boldsymbol{\Omega} = \boldsymbol{\Omega}^{\mathsf{T}}$. It has $N(M-1)$ eigenvalues of ones and N eigenvalues of zeros, since $\mathrm{rank}(\boldsymbol{\Omega}) = \mathrm{rank}(\mathbf{A}) = N(M - 1)$. Therefore, $\boldsymbol{\Omega}$ is positive semi-definite.

(ii) The matrix $\mathbf{M}$ is also an orthogonal projection matrix, and its eigenvalues consist of N ones and $N(M - 1)$ zeros [29]; therefore, it is positive semi-definite.

It follows from (ii) that

$$
\mathbf{B}_n(k)\mathbf{M}(k)\mathbf{B}_n^{\mathsf{T}}(k) \succeq \mathbf{0}. \tag{50}
$$

From (49) and (50), it can be concluded that

$$
\mathbf{P}_{\bar{\boldsymbol{r}}_{r_n}}(k|k) \succeq \mathbf{P}_{\boldsymbol{r}_{r_n}}(k|k). \tag{51}
$$

$\qquad \square$

C. Simulation Results

This subsection presents simulation results demonstrating Theorem IV.2 for an environment consisting of $N = 4$ UAV-mounted receivers and $M = 6$ SOP transmitters.

The UAVs' simulated trajectories included two straight segments, a climb, and a repeating orbit, performed over a 200 second period, which were generated using a standard six degree of freedom (DoF) kinematic model for airplanes [27]. The error-corrupted IMU data was set to correspond to a consumer grade IMU and was generated using the vehicles'

simulated specific forces and rotation rates through (3) and (4). Each UAV-mounted receiver was set to be equipped with a typical temperature-compensated crystal oscillator (TCXO), with $\{h_{0,r_n}, h_{-2,r_n}\}_{n=1}^4 = \{9.4 \times 10^{-20}, 3.8 \times 10^{-21}\}$.

GPS L1 C/A pseudoranges were generated at 1 Hz according to (6) using SV orbits produced from Receiver Independent Exchange (RINEX) files downloaded on October 22, 2016 from a Continuously Operating Reference Station (CORS) server [30]. Eleven satellites were set to be available ($L = 11$) for $t \in [0, 50)$ seconds, and unavailable ($L = 0$) for $t \in [50, 200]$ seconds. Pseudoranges were generated to the SOPs at 5 Hz according to (5) and the SOP dynamics discussed in Subsection II-A. Each SOP was set to be equipped with a typical oven-controlled crystal oscillator (OCXO), with $\{h_{0,\mathrm{sop}_m}, h_{-2,\mathrm{sop}_m}\}_{m=1}^6 = \{8 \times 10^{-20}, 4 \times 10^{-23}\}$. The SOP emitters' positions $\{\boldsymbol{r}_{\mathrm{sop},m}\}_{m=1}^6$ were surveyed from cellular tower locations in downtown Los Angeles, California. The simulated trajectories, SOP emitters' positions, and the UAVs' positions at the time GPS was set to become unavailable are illustrated in Fig. 2.
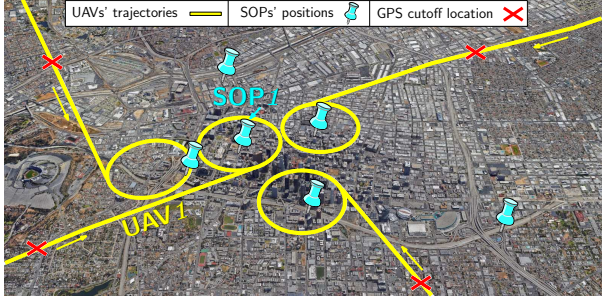

Fig. 2. True trajectories the UAVs traversed (yellow), SOP emitters' positions (blue pins), and the UAVs' positions at the time GPS was cut off (red).

The CoRSLAM information fusion strategies (1) TOA and (2) TDOA with SOP referencing, described in Subsection III-D and Subsection III-E, respectively, were compared. Errors for a traditional tightly-coupled GPS-aided INS are also provided for a comparative analysis. Fig. 3 shows the resulting estimation error trajectories and corresponding $\pm 3\sigma$ estimation error standard deviations for both strategies for the north, east, and down position states for UAV 1 and SOP 1. Fig. 4 illustrates the logarithm of the determinant of the estimation error covariance of the same UAV's position states, $\log\{\det[\mathbf{P}_{\boldsymbol{r}_{r_1}}]\}$, which is related to the volume of the uncertainty ellipsoid. It is worth mentioning that these are representative results. Similar behavior of the estimation error uncertainties in the position states was reported for the other UAVs and SOPs.

The following performance comparison may be concluded from these plots. First, the errors associated with the distributed SOP-aided INS, regardless of the CoRSLAM information fusion strategy remained bounded after GPS was cut off, whereas the errors associated with an unaided INS began to diverge. Second, the TOA information fusion strategy consistently produced lower $\log\{\det[\mathbf{P}_{\boldsymbol{r}_{r,1}}(k|k)]\}$ than the TDOA with SOP referencing for the entire UAV trajectory,
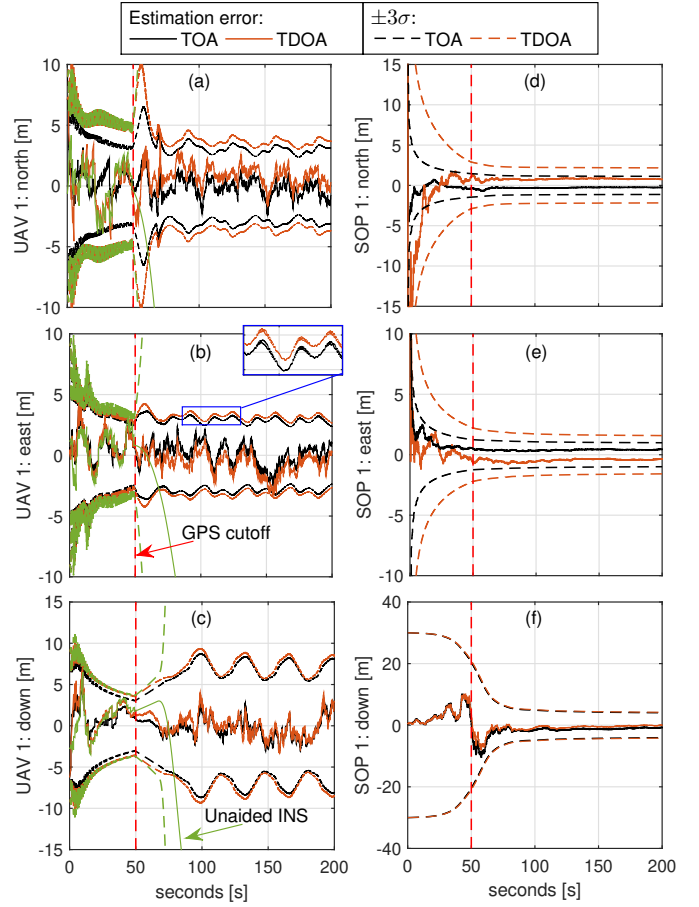

Fig. 3. Estimation error trajectories and $\pm 3\sigma$ bounds for the (1) TOA and (2) TDOA with SOP referencing information fusion strategies for the environment depicted in Fig. 2. (a)-(c) Correspond to UAV 1 north, east, and down position errors, respectively. (d)-(f) Correspond to SOP 1 north, east, and down position errors, respectively. The red dotted line marks the time GPS pseudoranges were set to become unavailable ($L = 0$).
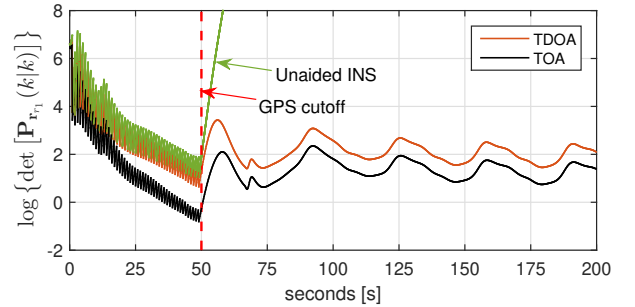

Fig. 4. The logarithm of the determinant of the position estimation error covariance of UAV 1 for the environment depicted in Fig. 2.

which included a straight segment, a banked turn, and a repeating orbit.

V. EXPERIMENTAL RESULTS

A field experiment was conducted using two UAVs equipped with consumer-grade IMUs and software-defined radios (SDRs) to demonstrate the TOA and TDOA information fusion strategies discussed in Section III. To this end, two

antennas were mounted on each UAV to acquire and track GPS signals and multiple cellular transmitters, whose signals were modulated through code division multiple access (CDMA). The GPS and cellular signals were simultaneously downmixed and synchronously sampled via two-channel Ettus® universal software radio peripherals (USRPs). These front-ends fed their data to the Multichannel Adaptive TRansceiver Information eXtractor (MATRIX) SDR, which produced pseudorange measurements from all GPS L1 C/A signals in view and three cellular transmitters [16]. The IMU data was sampled from the UAVs' on-board proprietary navigation system, which was developed by Autel Robotics®. Fig. 5(a) depicts the hardware and software setup and Fig. 5(b) illustrates the experimental environment.
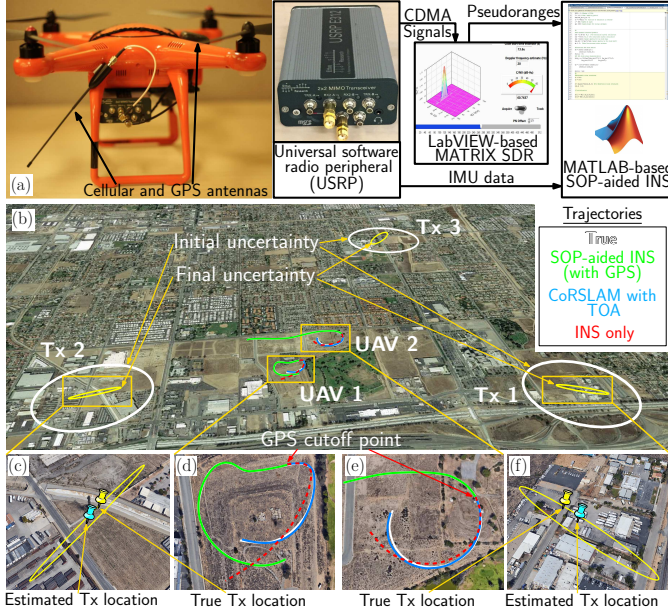

Fig. 5. (a) Experiment hardware setup. (b) Experimental environment with three cellular transmitters (Tx) and two UAVs. (c)-(f) Mapping and navigation results for CoRSLAM with TOA information fusion.

Experimental results are presented for three frameworks: (i) CoRSLAM with TOA information fusion, (ii) CoRSLAM with TDOA information fusion, as described in Section III and (iii) for comparative analysis, a traditional GPS-aided INS. The UAVs traversed the white trajectories plotted in Figs. 5(d)–(e), in which GPS was available for the first 50 seconds then unavailable for the last 30 seconds. The north-east root mean squared errors (RMSE) and final errors for all three frameworks for the UAVs are summarized in Table. I. The final estimated transmitter location and corresponding uncertainty for two of the transmitters are shown in Fig. 5(c) and Fig. 5(f). The final localization errors for the three transmitters were 9.0, 7.9, and 52.8 m, respectively. The north-east 99th-percentile initial and final uncertainty ellipses of the transmitter position states are illustrated in Fig. 5(b). Note that the relatively large estimation error of the third transmitter, which is attributed to poor receiver-to-transmitter geometry, is captured within the larger estimation uncertainty ellipse.

TABLE I
EXPERIMENTAL ESTIMATION ERRORS

Framework	GPS-aided INS		CoRSLAM-TOA		CoRSLAM-TDOA	
Vehicle	UAV 1	UAV 2	UAV 1	UAV 2	UAV 1	UAV 2
RMSE (m)	21.5	18.9	3.1	4.2	3.3	4.4
Final Error (m)	57.3	54.7	4.3	6.0	4.4	6.2

VI. CONCLUSION

This paper studied two information fusion strategies for CoRSLAM: TOA measurements and TDOA measurements with SOP referencing. It was shown that using TOA measurements results in smaller AVs' position estimation error covariance than using TDOA measurements, regardless of the selected SOP reference. Experimental results demonstrated two UAVs navigating with CoRSLAM using TOA measurements from three cellular transmitters in the absence of GPS, which yielded trajectory RMSE reductions of 85.6% for UAV 1 and 77.8% for UAV 2 when compared to unaided INSs.

REFERENCES

[1] J. Farrell and M. Barth, *Aided Navigation: GPS with High Rate Sensors*. New York: McGraw-Hill, 2008.

[2] A. Soloviev, "Tight coupling of GPS, INS, and laser for urban navigation," *IEEE Transactions on Aerospace and Electronic Systems*, vol. 46, no. 4, pp. 1731–1746, October 2010.

[3] M. Li and A. Mourikis, "High-precision, consistent EKF-based visual-inertial odometry," *International Journal of Robotics Research*, vol. 32, no. 6, pp. 690–711, May 2013.

[4] L. Merry, R. Faragher, and S. Schedin, "Comparison of opportunistic signals for localisation," in *Proceedings of IFAC Symposium on Intelligent Autonomous Vehicles*, September 2010, pp. 109–114.

[5] K. Pesyna, Z. Kassas, J. Bhatti, and T. Humphreys, "Tightly-coupled opportunistic navigation for deep urban and indoor positioning," in *Proceedings of ION GNSS Conference*, September 2011, pp. 3605–3617.

[6] Z. Kassas, "Collaborative opportunistic navigation," *IEEE Aerospace and Electronic Systems Magazine*, vol. 28, no. 6, pp. 38–41, 2013.

[7] S. Fang, J. Chen, H. Huang, and T. Lin, "Is FM a RF-based positioning solution in a metropolitan-scale environment? A probabilistic approach with radio measurements analysis," *IEEE Transactions on Broadcasting*, vol. 55, no. 3, pp. 577–588, September 2009.

[8] C. Yang, T. Nguyen, and E. Blasch, "Mobile positioning via fusion of mixed signals of opportunity," *IEEE Aerospace and Electronic Systems Magazine*, vol. 29, no. 4, pp. 34–46, April 2014.

[9] J. Khalife, K. Shamaei, and Z. Kassas, "A software-defined receiver architecture for cellular CDMA-based navigation," in *Proceedings of IEEE/ION Position, Location, and Navigation Symposium*, April 2016, pp. 816–826.

[10] K. Shamaei, J. Khalife, and Z. Kassas, "Exploiting LTE signals for navigation: Theory to implementation," *IEEE Transactions on Wireless Communications*, vol. 17, no. 4, pp. 2173–2189, April 2018.

[11] P. Thevenon, S. Damien, O. Julien, C. Macabiau, M. Bousquet, L. Ries, and S. Corazza, "Positioning using mobile TV based on the DVB-SH standard," *NAVIGATION, Journal of the Institute of Navigation*, vol. 58, no. 2, pp. 71–90, 2011.

[12] M. Joerger, L. Gratton, B. Pervan, and C. Cohen, "Analysis of Iridium-augmented GPS for floating carrier phase positioning," *NAVIGATION, Journal of the Institute of Navigation*, vol. 57, no. 2, pp. 137–160, 2010.

[13] K. Pesyna, Z. Kassas, and T. Humphreys, "Constructing a continuous phase time history from TDMA signals for opportunistic navigation," in *Proceedings of IEEE/ION Position Location and Navigation Symposium*, April 2012, pp. 1209–1220.

[14] J. Morales, P. Roysdon, and Z. Kassas, "Signals of opportunity aided inertial navigation," in *Proceedings of ION GNSS Conference*, September 2016, pp. 1492–1501.

[15] Z. Kassas, "Analysis and synthesis of collaborative opportunistic navigation systems," Ph.D. dissertation, The University of Texas at Austin, USA, 2014.

[16] J. Khalife, K. Shamaei, and Z. Kassas, "Navigation with cellular CDMA signals – part I: Signal modeling and software-defined receiver design," *IEEE Transactions on Signal Processing*, vol. 66, no. 8, pp. 2191–2203, April 2018.

[17] Z. Kassas and T. Humphreys, "Observability analysis of collaborative opportunistic navigation with pseudorange measurements," *IEEE Transactions on Intelligent Transportation Systems*, vol. 15, no. 1, pp. 260–273, February 2014.

[18] H. Mokhtarzadeh and D. Gebre-Egziabher, "Cooperative inertial navigation," *NAVIGATION, Journal of the Institute of Navigation*, vol. 61, no. 2, pp. 77–94, 2014.

[19] C. Yang and A. Soloviev, "Covariance analysis of spatial and temporal effects of collaborative navigation," *NAVIGATION, Journal of the Institute of Navigation*, vol. 61, no. 3, pp. 213–225, 2014.

[20] J. Morales and Z. Kassas, "Distributed signals of opportunity aided inertial navigation with intermittent communication," in *Proceedings of ION GNSS Conference*, September 2017, pp. 2519–2530.

[21] D. Shin and T. Sung, "Comparisons of error characteristics between TOA and TDOA positioning," *IEEE Transactions on Aerospace and Electronic Systems*, vol. 38, no. 1, pp. 307–311, January 2002.

[22] T. Sathyan, M. Hedley, and M. Mallick, "An analysis of the error characteristics of two time of arrival localization techniques," in *Proceedings of International Conference on Information Fusion*, July 2010, pp. 1–7.

[23] R. Kaune, "Accuracy studies for TDOA and TOA localization," in *Proceedings of International Conference on Information Fusion*, July 2012, pp. 408–415.

[24] A. Thompson, J. Moran, and G. Swenson, *Interferometry and Synthesis in Radio Astronomy*, 2nd ed. John Wiley & Sons, 2001.

[25] M. Shuster, "A survey of attitude representations," *The Journal of the Astronautical Sciences*, vol. 41, no. 4, pp. 439–517, October 1993.

[26] J. Farrell and M. Barth, *The Global Positioning System and Inertial Navigation*. New York: McGraw-Hill, 1998.

[27] P. Groves, *Principles of GNSS, Inertial, and Multisensor Integrated Navigation Systems*, 2nd ed. Artech House, 2013.

[28] J. Morales and Z. Kassas, "A low communication rate distributed inertial navigation architecture with cellular signal aiding," in *Proceedings of IEEE Vehicular Technology Conference*, 2018, accepted.

[29] T. Amemiya, *Advanced Econometrics*. Cambridge, Massachusetts: Harvard University Press, 1985, p. 460.

[30] R. Snay and M. Soler, "Continuously operating reference station (CORS): history, applications, and future enhancements," *Journal of Surveying Engineering*, vol. 134, no. 4, pp. 95–104, November 2008.